

# Oct 2010 Endcap Ring Alignment

Jim Pivarski

November 5, 2010

## Contents

<b>1</b>	<b>Motivation</b>	<b>1</b>
<b>2</b>	<b>Ring alignment procedure with tracks from the tracker</b>	<b>2</b>
2.1	Data samples . . . . .	2
2.2	Robust estimators and handling magnetic field errors . . . . .	3
<b>3</b>	<b>Tracker-to-ring alignment results</b>	<b>5</b>
3.1	Study of systematic errors . . . . .	6
3.2	Tests for additional dependencies . . . . .	10
3.3	Final results . . . . .	10
<b>4</b>	<b>Cross-check with independent beam-halo muons</b>	<b>12</b>
4.1	Quantifying magnetic field for beam-halo tracks . . . . .	16
4.2	Relative alignment datasets and method . . . . .	18
4.3	Cross-check results . . . . .	18
<b>5</b>	<b>Stability of internal chamber alignment</b>	<b>18</b>
<b>6</b>	<b>Conclusions: recommended endcap constants</b>	<b>27</b>
6.1	Provenance of set of constants . . . . .	30
6.2	Well-defined methods to repeat with the latest tracker and cross-alignments .	30

## 1 Motivation

The CSC ring positions currently used to reconstruct endcap muons are derived from  $p_T > 100$  GeV/ $c$  cosmic rays, which have incomplete information about the vertical positions of the rings due to the paucity of horizontal cosmic ray tracks. In addition, the method has been made significantly more robust due to new studies presented in this note. It is therefore worthwhile to re-align the rings using  $\phi$ -symmetric collisions data with the improved methods.

Two techniques will be described in this note: ring alignment relative to the tracker using tracks from collisions and ring alignment relative to one another, using the long “straight-through” beam-halo tracks that cross three or four stations. The first method is more complete and will be used for the final alignment. The second method will be used as a cross-check. Since the two methods use completely disjoint sets of tracks, they are statistically independent, and since the methods are so different, they share few systematic uncertainties.

## 2 Ring alignment procedure with tracks from the tracker

To align CSC rings relative to the tracker, we propagate tracker-tracks into the muon system and quantify the misalignment by the pattern of differences between propagated muon trajectories and observed muon hit positions (the residuals). The tracker-to-muon propagation was implemented by refitting GlobalMuon tracks with a negligible weight applied to the muon hits (AlignmentPositionError = (1000 cm)<sup>2</sup>), just like the Reference-Target algorithm. Results of this method will be compared with results obtained with re-reconstructed TrackerMuons, to check for any effect of the refitted-GlobalMuon/TrackerMuon discrepancies observed in Reference-Target studies on the bulk positions of rings.

If the rings are internally well-aligned (that is, if all chambers are correctly aligned relative to one another within each ring), then the expected pattern of residuals is a sine + cosine + constant curve as a function of  $\phi$ . The three constants from the fit are directly related to the translational position (global  $x$  and  $y$ ) and rotation angle around the beamline ( $\phi_z$ ). We apply these corrections to the ring orientation, leaving the internal chamber structure intact, and re-plot the residuals to confirm that our interpretation was correct. The final results are derived from two successive applications of the procedure, to verify that the procedure has reached self-consistency.

The explicit fit function of residuals versus  $\phi$  is

$$\phi_z^g(\phi) = \delta_x R \sin \phi - \delta_y R \cos \phi - \delta_{\phi_z} \quad (1)$$

- where  $\phi_z^g$  is the “ $\phi$  residual,” the difference between the propagated track and muon segment in  $\phi = \tan^{-1}(y/x)$ ;
- $\phi$  is the position of the muon segment (not the muon track at the origin);
- $R$  is the radius of the ring in question;
- $\delta_x$ ,  $\delta_y$ , and  $\delta_{\phi_z}$  are the explicit, global corrections to the geometry that make the system more aligned (with the above signs).

### 2.1 Data samples

The alignments presented here are based on almost 22 pb<sup>-1</sup> of collisions data, rather than cosmic rays. Collisions have the advantage of  $\phi$  symmetry, which is more important for characterizing a  $\phi$ -trend than high statistics in any single bin. Collisions have the disadvantage

of having lower typical momentum than cosmic rays. A study of high- and low-momentum cosmic rays was presented by Vadim at the Oct. 15 Muon Alignment meeting<sup>1</sup>.

The data lumi-sections were selected using the latest official JSON file from October 29, including runs 135821–144114 and 146428–148864 (CMS runs 2010A and part of 2010B). The integrated luminosity is  $3.1 \text{ pb}^{-1}$  (2010A) +  $18.8 \text{ pb}^{-1}$  (2010B) =  $21.9 \text{ pb}^{-1}$ . The explicit dataset names are

- /Mu/Run2010A-MuAlCalIsolatedMu-Sep17ReReco\_v2/ALCARECO
- /Mu/Run2010B-MuAlCalIsolatedMu-v2/ALCARECO

for refittable GlobalMuons and

- /Mu/Run2010A-Sep17ReReco\_v2/RECO
- /Mu/Run2010B-PromptReco-v2/RECO

for re-reconstructable TrackerMuons. The Sep17ReReco and 2010B-PromptReco correspond to the same set of conditions (alignments and calibrations).

In all cases, a  $p_T > 15 \text{ GeV}/c$  cut is applied to muons to avoid the changing unprescaled trigger threshold (from 5 to 9  $\text{GeV}/c$  in 2010A to 11  $\text{GeV}/c$  in 2010B).

## 2.2 Robust estimators and handling magnetic field errors

Residuals are biased by several effects other than alignment, and these must be properly accounted for. The largest effects are

- non-multiple scattering, which gives rise to non-Gaussian tails in the residuals distribution;
- material budget and magnetic field errors, which bias the residuals peak with equal magnitude in opposite directions for positively and negatively charged muons;
- pion to muon decay-in-flight in which the pion and muon are incorrectly identified as a single track with a kink outside of the tracker volume.

The first two sources of systematic error are familiar from cosmic-ray alignments, and we apply well-established techniques to minimize our sensitivity to them. The third source is unique to muons from collisions. We verify that decays-in-flight have negligible effect on the ring placement through the cross-check with “straight-through” beam-halo muons, a sample which contains no decays-in-flight.

Figure 1 illustrates the non-Gaussian tails from non-multiple scattering and/or decays-in-flight. In the Reference-Target algorithm, these tails are controlled by modifying the fit function to include a non-Gaussian component; here, we simply perform a restricted Gaussian fit of the peak in multiple passes. In the first pass, residuals within  $(-RMS, +RMS)$  are included in the fit; in a subsequent pass, residuals within  $(-\sigma, +\sigma)$  of the previous fit are included.

---

<sup>1</sup><http://indico.cern.ch/conferenceDisplay.py?confId=110638>

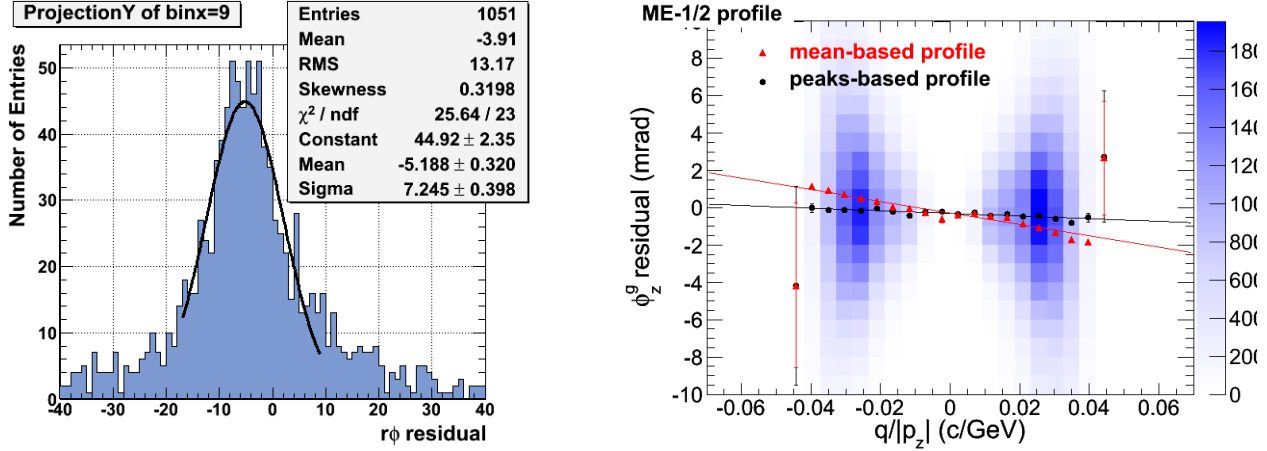


Figure 1: Left: residuals histogram illustrating the large non-Gaussian tails and restricted Gaussian fit to identify the peak position. Right: residuals versus  $q/|p_z|$  with points determined by the mean of vertical slices (red) and points determined by the restricted Gaussian peak-fits (black).

The non-Gaussian tails have a strong dependence on charge-over-momentum,  $q/p_T$  and  $q/|p_z|$ , also shown in Fig. 1. This is expected for scattering but not for decays-in-flight, indicating that a significant fraction of the tails are due to scattering.

**Magnetic field errors: to be filled in later.** *In the most up-to-date set of plots, I (Jim) don't see conclusive evidence of magnetic field errors: the difference between positive and negative muons far from the beamline could just as easily be a material budget error. The distinction would be seen in the residuals versus  $q/p_T$  (for axial magnetic field errors) and  $q/|p_z|$  (for radial magnetic field errors): if these are linear and primarily affect the peak of the residuals, then they are consistent with being magnetic field errors; if the effect is significantly larger for low-momentum muons and especially affects the tails (which seems to be demonstrated by Fig. 1-b), then they are more consistent with material budget errors. Ultimately, we won't be able to precisely map the material or magnetic field with this technique because there are more free parameters than observables (e.g. a charge-dependent bias that grows with distance from the beamline might be a constant radial magnetic field error and our hard  $p_T$  cut or a radially-varying axial magnetic field error), but we can cancel the effect by extracting the charge-symmetric residuals bias. (end FIXME).*

To cancel the effect of any possible magnetic field error or material budget error, we extract the charge-symmetric part of the residuals bias. Magnetic field and material budget errors bias residuals in equal and opposite directions for positively and negatively charged muons of the same momentum, a charge-antisymmetric effect. Misalignments, on the other hand, are independent of the charge of the muons that are used to probe them. Thus, we can cleanly separate the misalignments from all charge-antisymmetric effects with a polynomial fit as a function versus  $q/p_T$  or  $q/|p_z|$ ; in practice, the function is linear so only the intercept (charge-symmetric) and slope (charge-antisymmetric) terms are relevant. Alternatively, we can plot the residuals peak separately for positively and negatively charged muons to graphically depict the average and deviation. Both are shown in Fig.2.

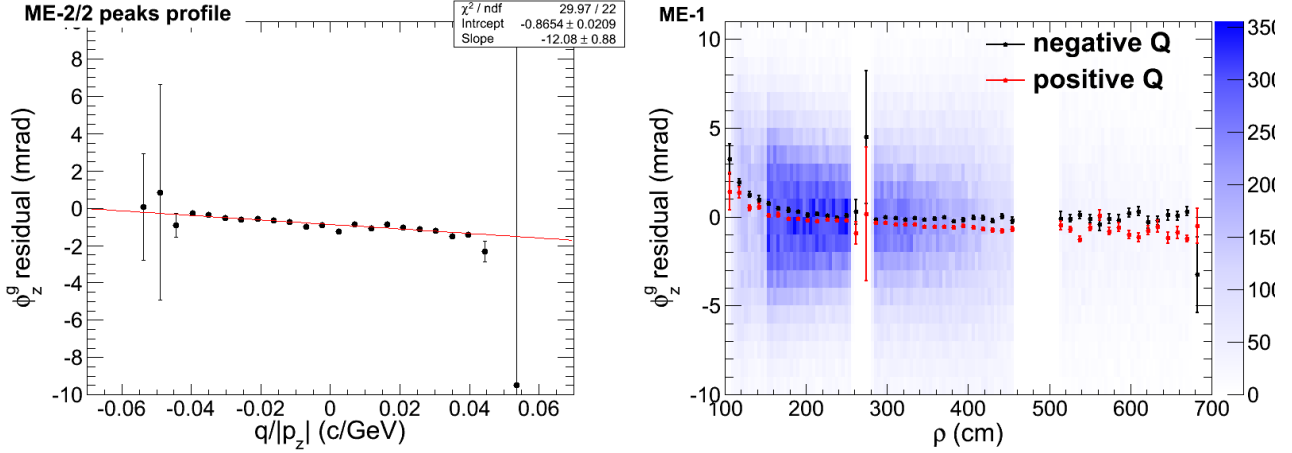


Figure 2: Left: residuals versus  $q/|p_z|$ , indicating what might be a small radial magnetic field error (the slope), and a  $-0.86 \text{ mrad} \times R$  misalignment (the intercept). Right: residuals for positively and negatively charged muons as a function of distance from the beamline  $\rho$ .

With these corrections for robustness, the final procedure is the following:

1.  $1\text{-}\sigma$  peak fit of  $\phi_z^g$  residuals in  $q/|p_z|$  and  $\phi$  bins ( $\phi$  of the segment, not the track at the origin);
2. linear fit of residuals-peaks versus  $q/|p_z|$  in  $\phi$  bins to determine the charge-symmetric part (the intercept);
3. plot the charge-symmetric part versus  $\phi$ , fit with Eqn. 1;
4. interpret the results of the fit as ring misalignments and correct the geometry;
5. repeat the whole procedure; the process converges within two iterations.

ME+4/2, will be treated specially because it contains only five chambers; it is not a  $\phi$ -symmetric ring. Of the three fit parameters in Eqn. 1, only  $\delta_{\phi_z}$  is independently fitted for ME+4/2;  $\delta_x$  and  $\delta_y$  are copied from ME+4/1. In ME1/1, all corresponding “a” and “b” chambers are treated as single objects for collecting residuals and applying alignment corrections.

### 3 Tracker-to-ring alignment results

A sample “map-plot” (residuals vs.  $\phi$ ) is shown for ME–2/1 in Fig. 3, before any alignment (ideal ring position). **FIXME: we need to see all of these, before and after alignment!** Plots of residuals in the other projection, residuals versus  $\rho$ , are shown in Fig. 4 after ring alignment. The special case of ME+4/2 is shown in Fig. 5 before alignment (ideal ring positions). Tables and plots of the resulting corrections will be presented at the end of this section, after describing how systematic uncertainties were calculated.

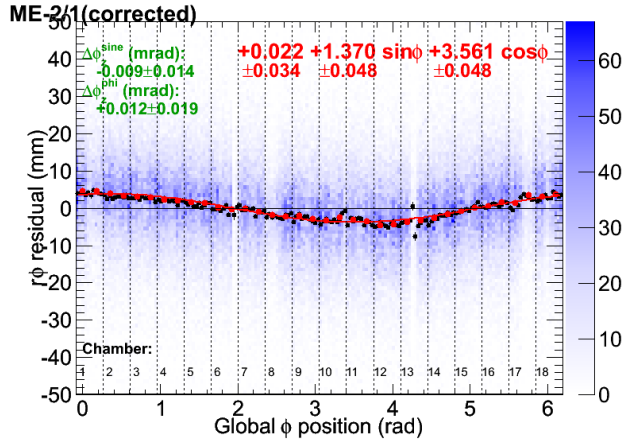


Figure 3: Residuals versus  $\phi$  for ME–2/1, where the residuals have been carefully fitted to determine the peaks and to cancel charge-antisymmetric biases. The collisions data are  $\phi$ -symmetric and cleanly describe a single sinusoidal curve.

### 3.1 Study of systematic errors

Two methods were used to quantify the systematic errors in the alignment, both quantifying the deviations of the residuals distribution from what would be expected for a single rigid ring. One quantifies the variation of the residuals in  $\rho$ , and the other quantifies the variation in  $\phi$ . The  $\rho$  variation is the dominant systematic uncertainty.

The  $\rho$  systematic starts with the observation that even the muon-antimuon average residual is not a constant with respect to  $\rho$ . This can be seen in Fig. 4, but it is highlighted for an extreme case (ME–1) in Fig. 6. This can be caused by coherent  $\phi_z$  misalignments in the internal alignment of the rings using beam-halo along the chamber overlaps: the overlaps measurements are only sensitive to *differences* in  $\phi_z$  misalignment between neighboring pairs of chambers, so a pure beam-halo alignment can only result in all chambers having the same  $\phi_z$  misalignment. This is mitigated by the fact that the internal alignments combine beam-halo and photogrammetry data, which resolves this last degree of freedom. However, the effect of any remaining  $\phi_z$  rotation would be amplified in this plot by the fact that all chambers have the same rotation angle. This internal misalignment makes the definition of a correct ring alignment ambiguous: should we align the bottoms of the chambers (edge closest to the beamline) or the tops? Averaging all residuals would yield a result that depends on the  $\eta$  distribution of the source. Therefore, difference between the minimum and the maximum is taken to be a systematic uncertainty.

The second systematic uncertainty allows for deformations in the circularity of the ring, also due to possible internal misalignments. Each ring is divided into four different half-ring subsets and re-fitted with Eqn. 1, as shown in Fig. 7. Deviations in the  $r\phi$  structure of the ring from a perfect circle would result in different  $\delta_x$ ,  $\delta_y$ ,  $\delta_{\phi_z}$  solutions: differences from the full-ring fit are taken as an additional systematic uncertainty. The uncertainties from  $\rho$  variations are much larger than the uncertainties from these  $\phi$  variations.

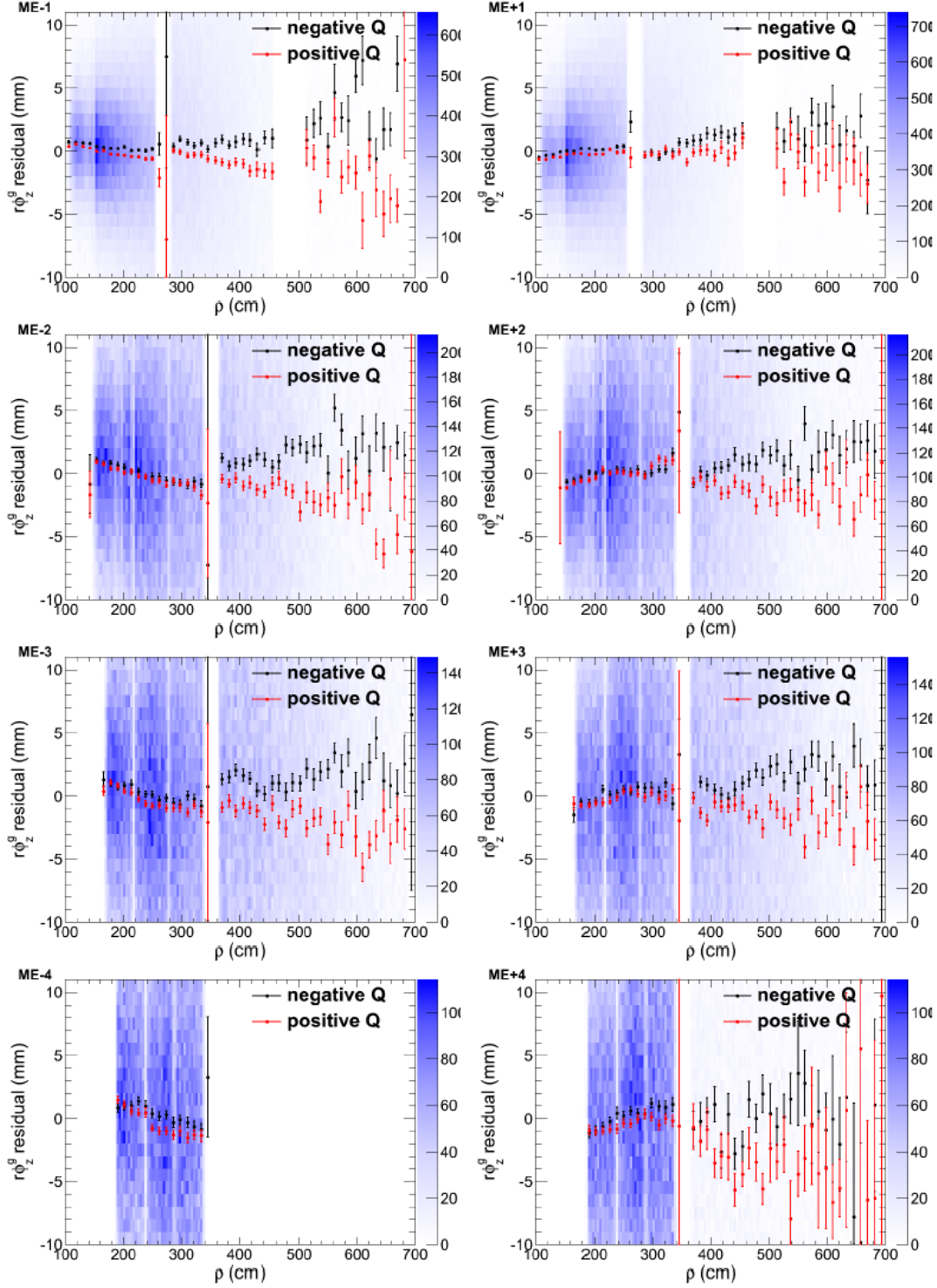


Figure 4: Residuals ( $r\phi$ , in mm) versus distance from the beamline  $\rho$  *after* ring-alignment. There is a clear, consistent separation between positively and negatively charged muons that grows with  $\rho$ . **But is it magnetic field or material? It would be interesting to see  $q/p_T$  and  $q/|p_z|$  in this region with proper momentum cuts (e.g. a  $p_T$  cut over a range of  $\rho$  would cut a triangular region out of  $q/|p_z|$  and bias the resulting picture).**

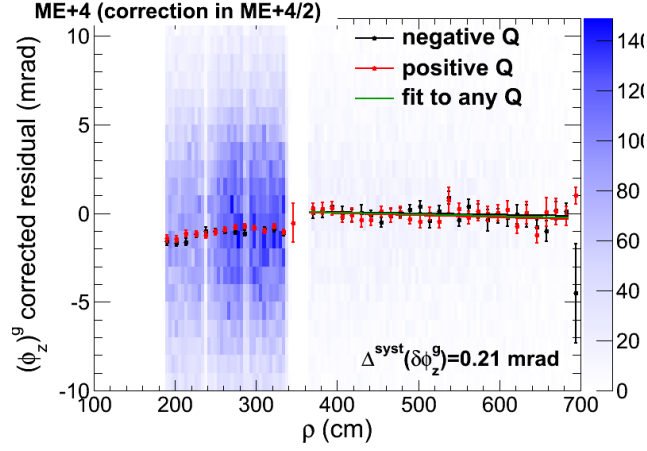


Figure 5: Residuals versus  $\rho$  in ME+4, showing the difference between ME+4/1 ( $200 < \rho < 340$  cm) and ME+4/2 ( $340 < \rho < 700$  cm), before alignment. A single-parameter ( $\delta\phi_z$ ) correction is made between the two rings.

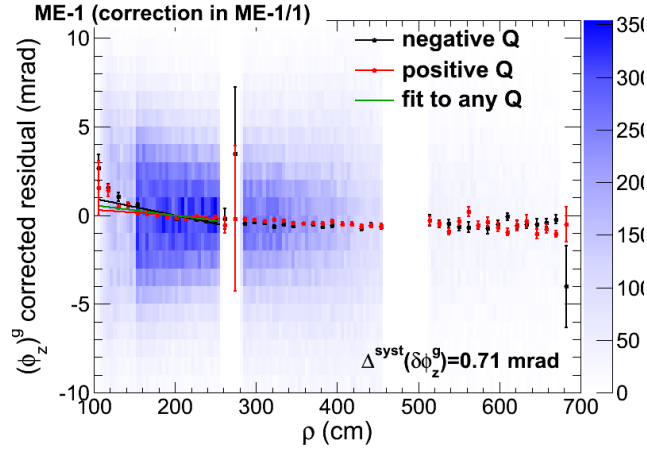


Figure 6: Residuals versus  $\rho$  for ME-1, showing the linear slope in ME-1/1. Either the  $\rho = 100$  cm edge or the  $\rho = 260$  cm edge could be aligned to zero, or something in between, so we take the difference in residuals between the two edges as a systematic uncertainty in the position of the ring.



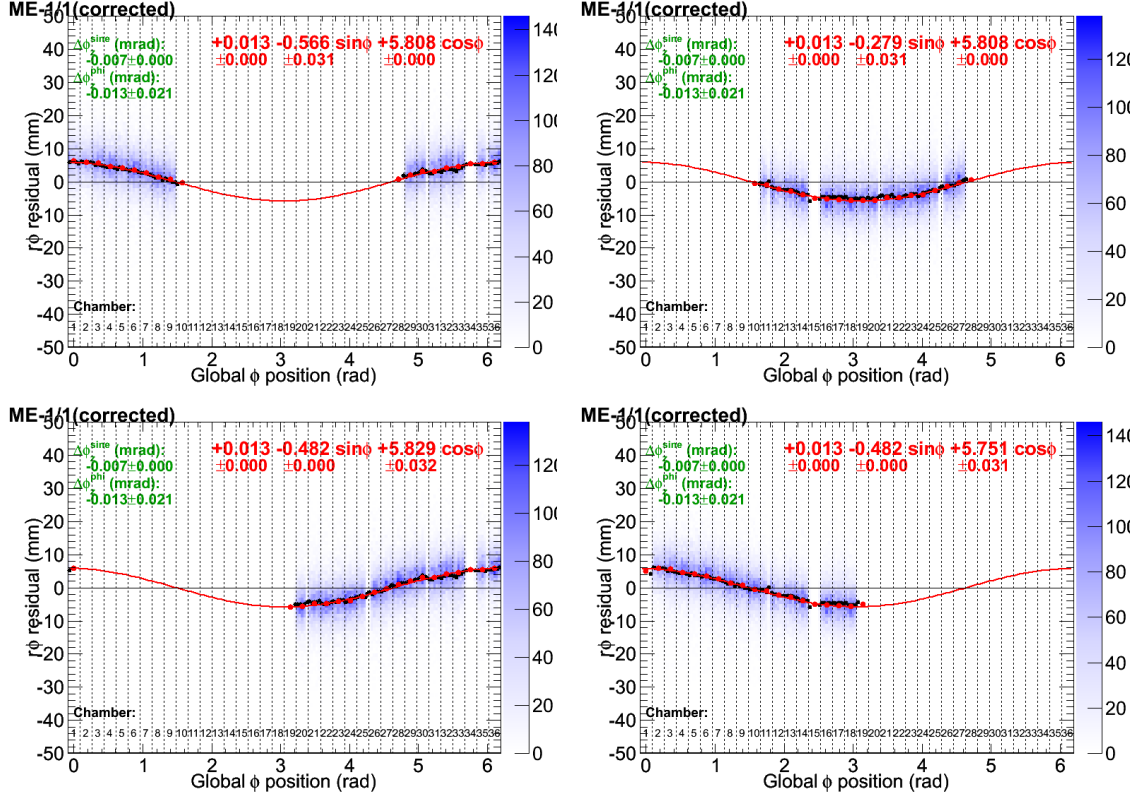


Figure 7: The ME-1/1 ring alignment determined by four different half-ring subsets. If the residuals deviate from a sinusoidal curve due to internal misalignments, it would result in different  $\delta_x$ ,  $\delta_y$ ,  $\delta_{\phi_z}$  solutions: this is taken as a second systematic uncertainty.

### 3.2 Tests for additional dependencies

The alignment of the previous section was tested in two additional ways: by changing the internal ring geometry and by changing the method used to calculate residuals. Plots illustrating the results of both will be shown in the next section.

Two internal alignments from beam-halo overlaps were delivered on Oct. 29; in one fit, all photogrammetry constraints were applied (“BHPG” for beam-halo and photogrammetry) and in the other, photogrammetry was only used to fill missing beam-halo data (“BHPG-holes” for beam-halo with photogrammetry “filling the holes”). The decision on an optimal internal alignment method was deferred until the completion of the ring-position alignment, to see if a difference in residuals from the tracker could be observed. Both internal alignments yield smooth rings; they differ in final ring alignment positions by 2 mm in  $ME+3/2 \delta_y$ , 0.5 mm in  $ME-3/2 \delta_x$ , all others are small (see Fig. 13 in the Oct. 29 HyperNews paper; this is the same pattern as was seen in the internal plots, though with a different magnitude). Differences in the global offset of the internal alignment is irrelevant because the global offset is corrected by the ring-alignment procedure described in this note—the only difference is in the pre-alignment initial condition. Therefore, the choice between internal alignments is arbitrary, and I would recommend the BHPGholes alignment, since it makes the minimum-necessary use of photogrammetry.

Another important test is to check for differences between refitted-GlobalMuons and re-reconstructed TrackerMuons in defining the residuals. The two methods ought to be equivalent, but differences have been observed within individual chambers in the Reference-Target alignment of the barrel. These differences may be irrelevant in the large-structure quantities  $\delta_x$ ,  $\delta_y$ , and  $\delta_{\phi_z}$ , so the ring-alignment was performed using both methods, with final results compared in the next section. Intermediate plots of residuals versus  $\rho$  and  $q/|p_z|$  are presented in Fig. 8. Differences in the final results are negligible compared to other systematic uncertainties.

### 3.3 Final results

Final results with systematic uncertainties are listed in Table 1. These results were computed using the “beam-halo with photogrammetry only filling holes” internal alignment and re-reconstructed TrackerMuon residuals described in Sec. 3.2. They are not corrections relative to what is currently in the database, but corrections relative to ideal ring positions. **(Differences with respect to what is currently in the database are desirable, but not yet available. To avoid interpretation errors from simply comparing this table to a table presented mid-summer, one should perform an alignment starting from the mid-summer geometry. However, that geometry lacks important internal-ring alignment corrections. The only rigorous comparison is at the level of individual chambers.)** These values are plotted in Figs. 9 and 10 with side-by-side comparisons of the two internal geometries and the two methods of calculating residuals. Corrections in the second iteration are shown to be small in Fig. 11, demonstrating that the procedure has converged.

Table 1: Table of final ring-alignment corrections relative to ideal. The first uncertainty is statistical (returned by the fitter) and the second is systematic, the sum of systematic error estimates from Sec. 3.1.

	$\delta_x$ (mm)	$\delta_y$ (mm)	$\delta_{\phi_z}$ (mrad)
ME+4/2	+0.86 $\pm$ 0.09 $\pm$ 0.61	+5.33 $\pm$ 0.09 $\pm$ 0.67	-1.28 $\pm$ 0.06 $\pm$ 0.21
ME+4/1	+0.86 $\pm$ 0.09 $\pm$ 0.61	+5.33 $\pm$ 0.09 $\pm$ 0.67	-0.27 $\pm$ 0.03 $\pm$ 0.39
ME+3/2	-0.16 $\pm$ 0.12 $\pm$ 1.85	-0.94 $\pm$ 0.12 $\pm$ 2.50	-0.09 $\pm$ 0.02 $\pm$ 0.27
ME+3/1	+0.03 $\pm$ 0.07 $\pm$ 0.30	+0.15 $\pm$ 0.07 $\pm$ 0.51	+0.28 $\pm$ 0.02 $\pm$ 0.31
ME+2/2	+0.57 $\pm$ 0.11 $\pm$ 1.46	+0.59 $\pm$ 0.11 $\pm$ 1.69	+0.06 $\pm$ 0.02 $\pm$ 0.27
ME+2/1	+0.31 $\pm$ 0.05 $\pm$ 0.32	-0.24 $\pm$ 0.05 $\pm$ 0.39	+0.32 $\pm$ 0.02 $\pm$ 0.42
ME+1/3	+4.35 $\pm$ 0.35 $\pm$ 0.57	+3.37 $\pm$ 0.34 $\pm$ 0.10	-0.00 $\pm$ 0.05 $\pm$ 0.15
ME+1/2	+3.56 $\pm$ 0.07 $\pm$ 1.31	+1.71 $\pm$ 0.07 $\pm$ 1.94	+0.21 $\pm$ 0.02 $\pm$ 0.27
ME+1/1	+4.30 $\pm$ 0.02 $\pm$ 0.46	-2.10 $\pm$ 0.02 $\pm$ 0.40	+0.03 $\pm$ 0.02 $\pm$ 0.57
ME-1/1	-0.48 $\pm$ 0.02 $\pm$ 0.14	-5.81 $\pm$ 0.02 $\pm$ 0.04	-0.14 $\pm$ 0.02 $\pm$ 0.71
ME-1/2	+0.87 $\pm$ 0.06 $\pm$ 0.76	-2.97 $\pm$ 0.06 $\pm$ 0.89	+0.30 $\pm$ 0.02 $\pm$ 0.20
ME-1/3	+0.83 $\pm$ 0.33 $\pm$ 0.06	-2.57 $\pm$ 0.37 $\pm$ 0.17	+0.41 $\pm$ 0.04 $\pm$ 0.21
ME-2/1	+1.37 $\pm$ 0.05 $\pm$ 0.51	-3.56 $\pm$ 0.05 $\pm$ 0.43	+0.54 $\pm$ 0.02 $\pm$ 0.56
ME-2/2	+1.79 $\pm$ 0.11 $\pm$ 1.13	-2.76 $\pm$ 0.11 $\pm$ 1.47	+0.87 $\pm$ 0.02 $\pm$ 0.21
ME-3/1	+2.07 $\pm$ 0.07 $\pm$ 0.41	-4.72 $\pm$ 0.07 $\pm$ 0.20	+0.47 $\pm$ 0.02 $\pm$ 0.52
ME-3/2	+3.16 $\pm$ 0.12 $\pm$ 0.03	-3.51 $\pm$ 0.12 $\pm$ 1.06	+0.90 $\pm$ 0.02 $\pm$ 0.17
ME-4/1	-0.02 $\pm$ 0.09 $\pm$ 0.31	-4.84 $\pm$ 0.09 $\pm$ 0.12	+0.19 $\pm$ 0.03 $\pm$ 0.63

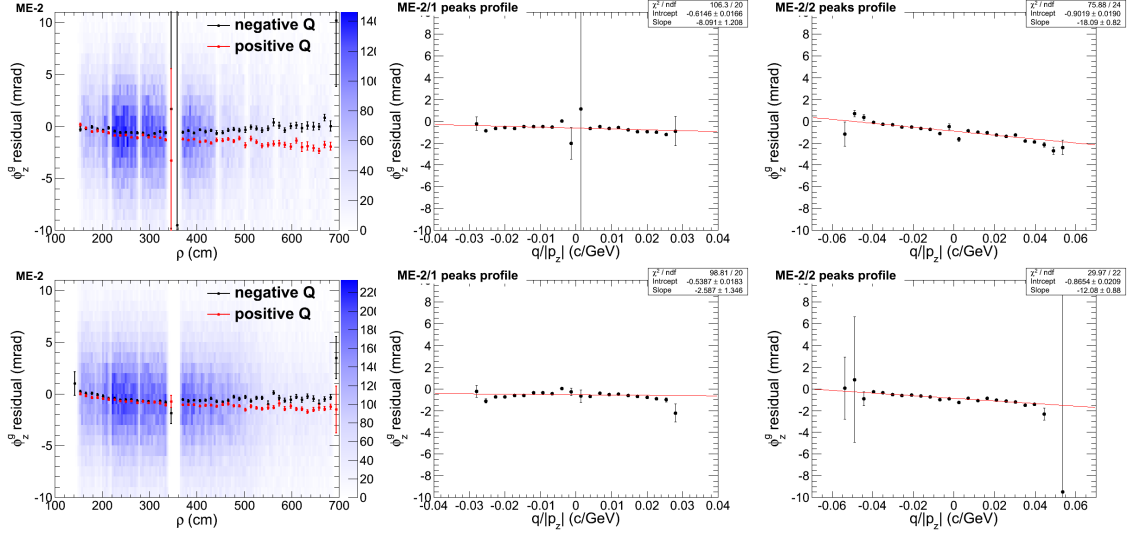


Figure 8: Top row: residuals from refitted-GlobalMuons (versus  $\rho$  and  $q/|p_z|$  for an inner and an outer ring). Bottom row: same for re-reconstructed TrackerMuons. The charge-splitting is slightly larger for GlobalMuons.

## 4 Cross-check with independent beam-halo muons

Muons from collisions currently provide the best alignment of endcap rings by aligning each ring relative to the tracker. However, it is also possible to align rings relative to one another using beam-halo muons. These muons are horizontal, do not cross the tracker, and typically have higher momentum than muons from collisions (since they originate in an LHC “fixed target experiment” with collimators upstream of CMS). The fact that these muons are parallel to the largest component of the CMS magnetic field complicates the momentum measurement, and the fact that they do not cross the tracker makes it impossible to align them to that reference. However, they provide a nice cross-check of the standard ring alignment, since the “absolute” tracker-to-ring alignment method should automatically yield a good “relative” ring-to-ring geometry.

Though both alignment procedures use tracks, they use disjoint sets of tracks in very different ways. No collisions muons are beam-halo muons and vice-versa, a fact that is guaranteed by cuts on the polar angles of the two samples:  $|\eta| < 2.4$  for collisions and  $|dr/dz| < 0.12$  for beam-halo— see Fig. 5 of the Oct. 29 HyperNews paper. The differences in method are the following:

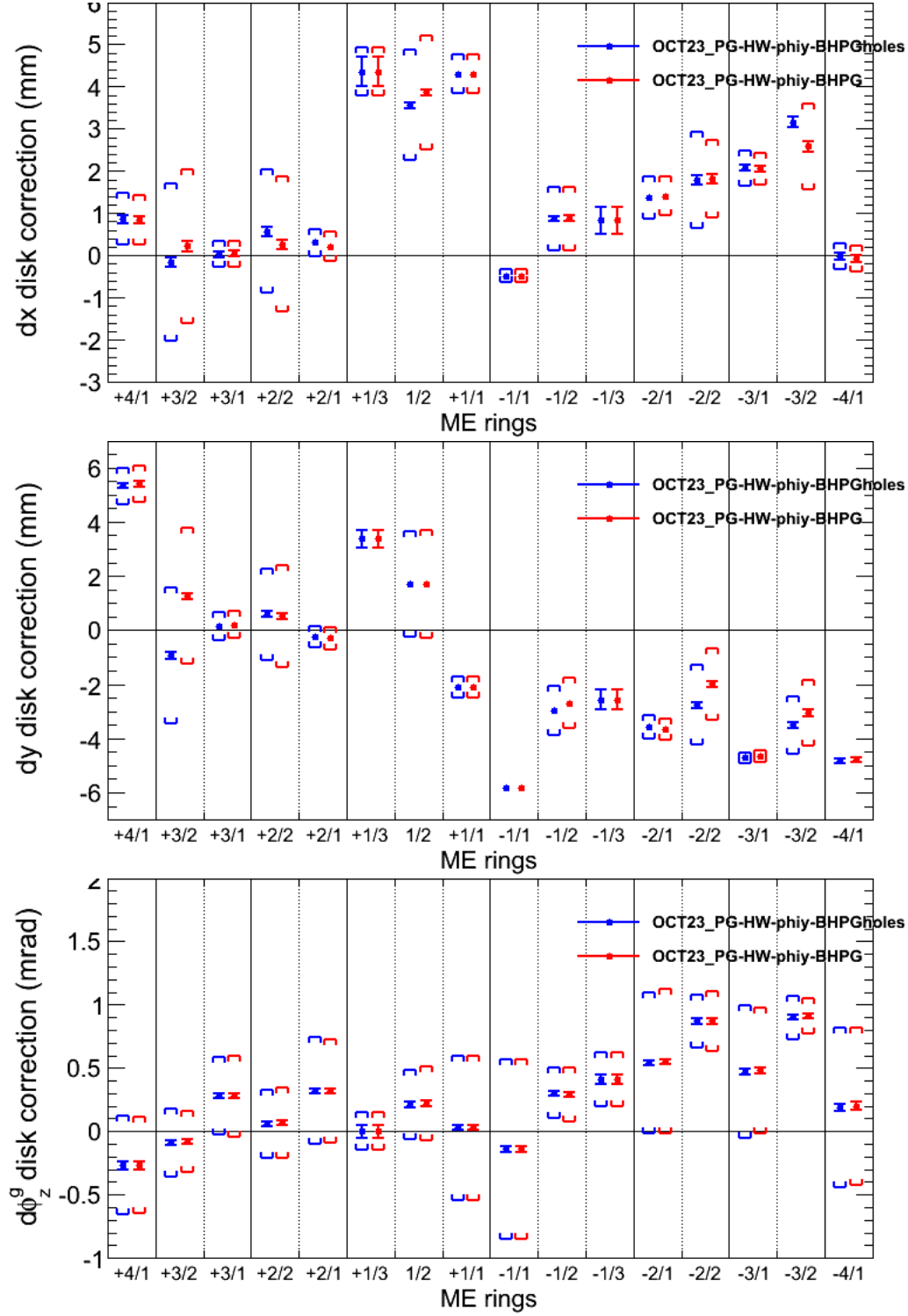


Figure 9: Final alignment quantities  $\delta_x$  (top),  $\delta_y$  (middle), and  $\delta_{\phi_z}$  (bottom) for all rings, computed using re-reconstructed TrackerMuons. The error bars represent statistical and the brackets represent systematic uncertainties. The two colors indicate differences between results using the “photogrammetry only filling holes” internal alignment (BHPGholes, blue) and the “all photogrammetry constraints” internal alignment (BHPG, red); both described in Sec. 3.2.

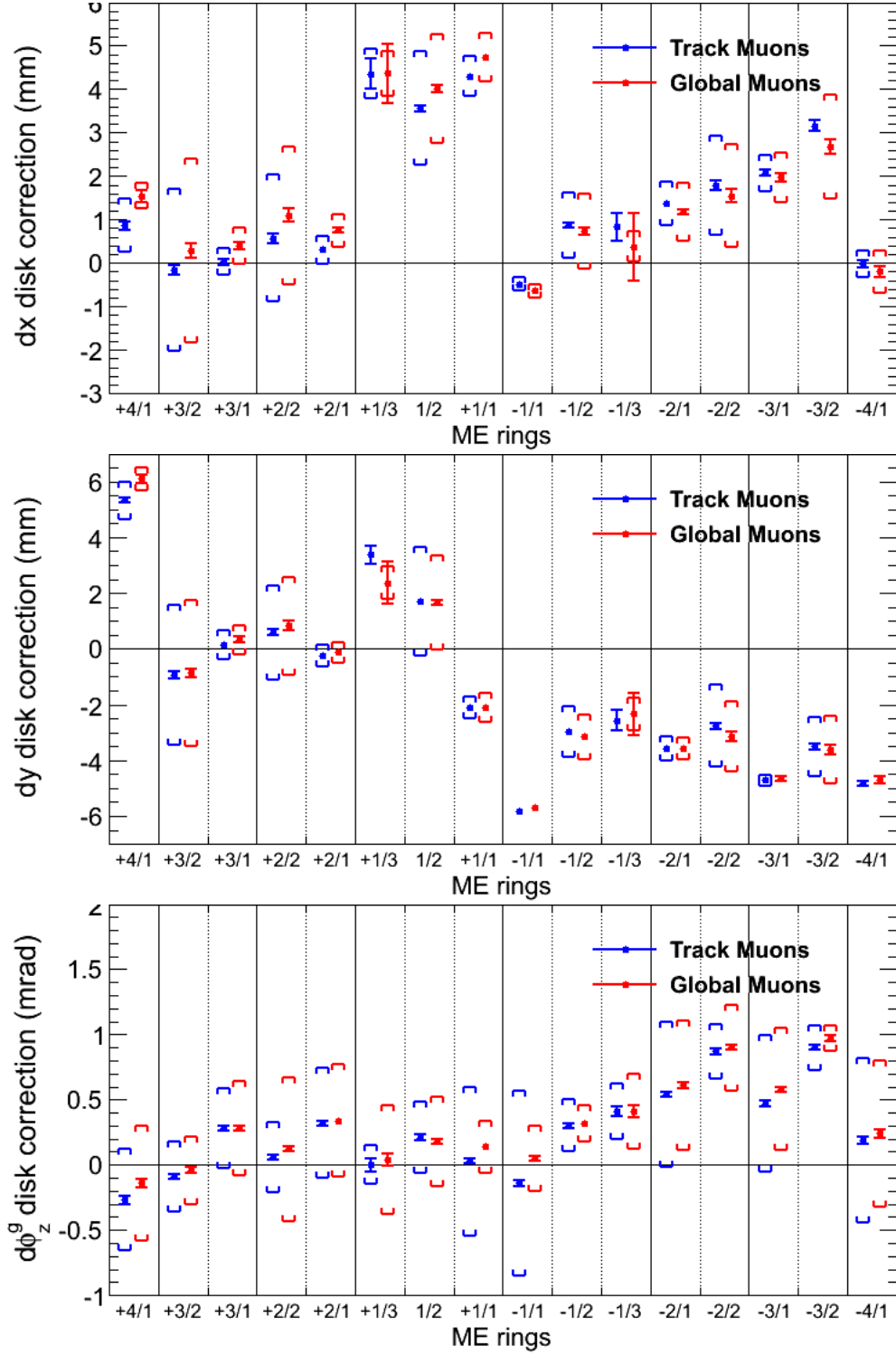


Figure 10: Final alignment quantities  $\delta_x$  (top),  $\delta_y$  (middle), and  $\delta_{\phi_z}$  (bottom) for all rings, computed using the “photogrammetry only filling holes” internal alignment. The error bars represent statistical and the brackets represent systematic uncertainties. The two colors indicate differences between results using re-reconstructed TrackerMuons (blue) and refitted-GlobalMuons (red); both described in Sec. 3.2.

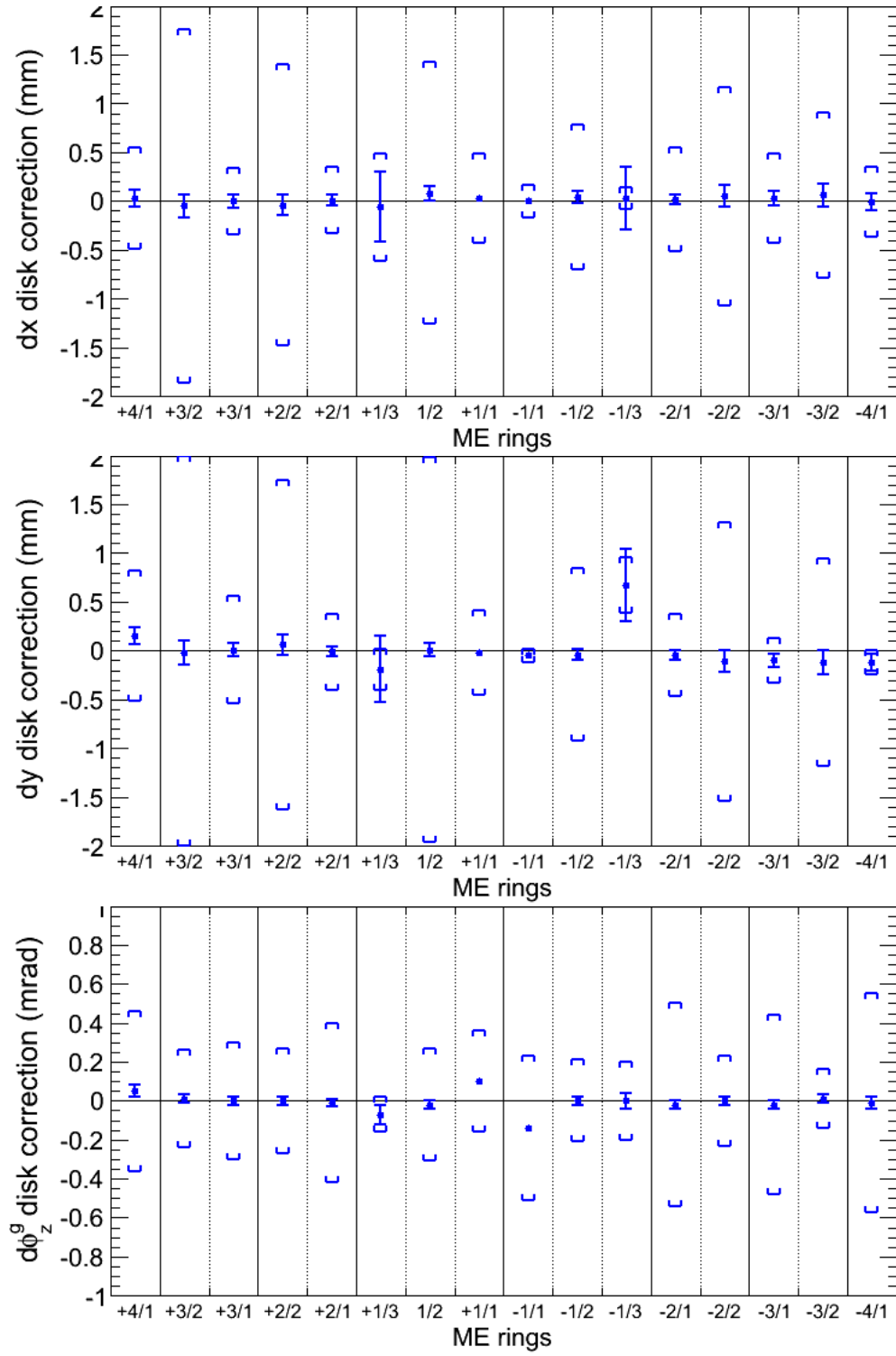


Figure 11: Changes in ring alignment parameters (top:  $\delta_x$ , middle:  $\delta_y$ , and bottom:  $\delta_{\phi_z}$ ) in the second application of the procedure, demonstrating that the procedure has converged.

Tracker-to-ring (collisions)	Ring-to-ring (beam-halo)
<ul style="list-style-type: none"> <li>• track parameters determined by tracker;</li> <li>• full propagation through CMS magnetic field and material;</li> <li>• correction for magnetic field material errors with a <math>q/ p_z </math> fit;</li> <li>• best results close to the tracker, where the propagation is shortest.</li> </ul>	<ul style="list-style-type: none"> <li>• “track parameters” determined by one segment;</li> <li>• linear extrapolation from one station to the next;</li> <li>• correction for assuming zero field with an average of <math>\mu^+</math> and <math>\mu^-</math> results;</li> <li>• best results far from the tracker, where the magnetic field is weakest.</li> </ul>

Thus, the beam-halo alignment makes a nice cross-check on the collisions alignment, particularly in ME4/1, where the tracker-tracks have been propagated the farthest and the beam-halo tracks are minimally affected by magnetic fields.

## 4.1 Quantifying magnetic field for beam-halo tracks

The velocity vector of beam-halo tracks is parallel to the axial magnetic field, so they are not affected by the magnetic field in the way that was designed for momentum measurement. However, in the CMS endcap, the radial magnetic field is strong enough to perform a rough estimate of beam-halo momentum, useful for rejecting low-momentum muons, which have wide residuals distributions. To construct an estimator independent of the ring positions themselves and avoid a circular dependency, we compute the momentum from changes in muon direction only, not position. (In the tracker-to-ring method, this independence derives from the fact that the momentum-measuring detector, the tracker, is distinct from the detector being aligned, the muon system.) Changes in a track’s  $d\phi/dz$  entrance angle are observed in three or four muon stations from the directions of the muon segments. The charge-times-momentum is

$$q \times p_z = \frac{B_r}{330 \text{ cm T/GeV}} (d\phi/dz)^{-1}. \quad (2)$$

With this definition of momentum, note that we cannot distinguish muons travelling in the  $+z$  direction from antimuons travelling in the  $-z$  direction. Without a known origin for the muons (such as the beamspot), the two cases can only be distinguished by energy loss in material, which we are not including in this simple calculation. However, most muons observed in the plus endcap are travelling in the  $-z$  direction and most muons observed in the minus endcap are travelling in the  $+z$  direction because CMS (in the lateral direction) is a powerful attenuator for muons.

Figure 12 presents Monte Carlo studies of this momentum estimator for the three-station case (ME1–3) and the four-station case (additionally including ME4/1). Though the momentum resolution is poor, an estimated- $p_z$  cut of 50 GeV/ $c$  is sufficient for eliminating muons with less than a few tens of GeV/ $c$ . Figure 13 shows the distribution of real beam-halo momentum, as determined by the three-station estimator.



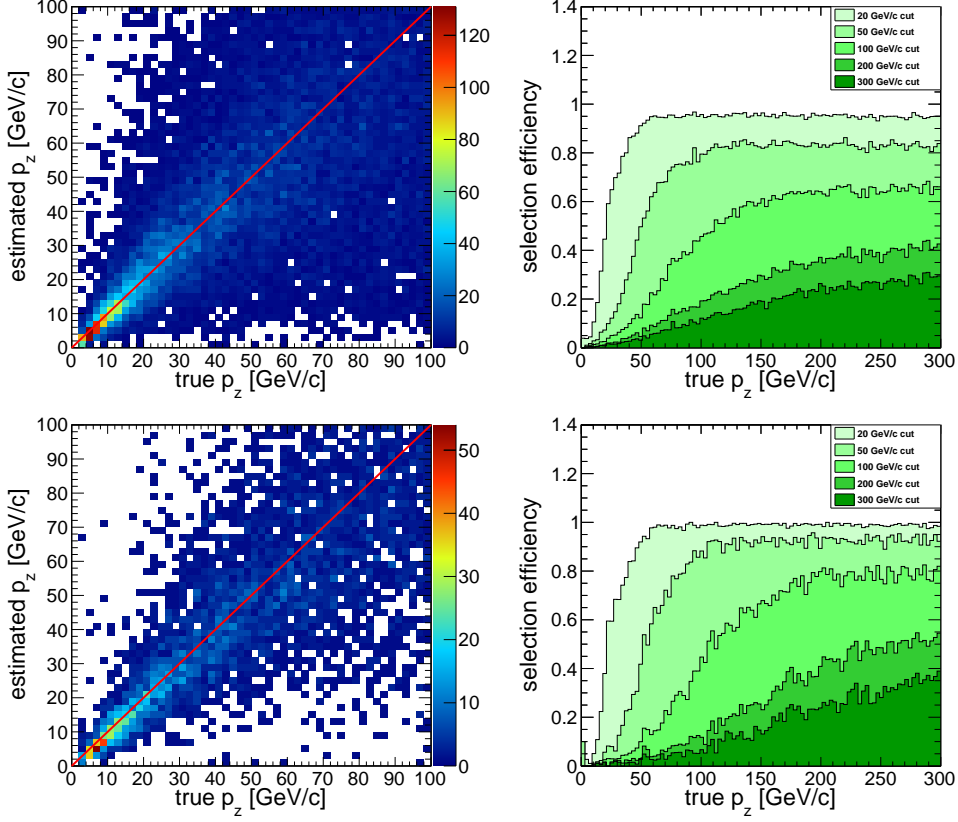


Figure 12: Momentum estimators of beam-halo muons studied in Monte Carlo; top: three-station estimator (ME1–3), bottom: four-station estimator. Left: estimated  $p_z$  compared to true  $p_z$ . Right: efficiency versus true  $p_z$  for various estimator- $p_z$  cuts. In this analysis, we required a three-station  $p_z > 50$  GeV/ $c$  cut when studying relative alignments of ME1–3 and a four-station  $p_z > 50$  GeV/ $c$  cut when studying the alignment of ME4/1 relative to ME3/1.

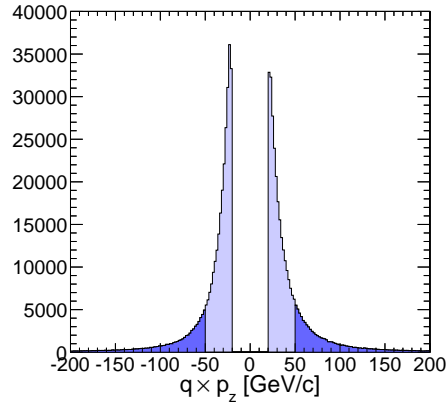


Figure 13: Momentum distribution of real beam-halo data with cuts at 20 and 50 GeV/ $c$  (three-station estimator).

## 4.2 Relative alignment datasets and method

The dataset used here was derived from a special trigger and AlCaReco stream to collect beam-halo muons during collisions. It includes data from mid-June (when single-beam intensities became sufficiently large) until Sep. 1 (when the trigger was retired). The AlCaReco stream is `/Cosmics/Run2010A-MuAlBeamHalo-v4/ALCARECO`. We applied a  $|p_z| > 50$  GeV/ $c$  cut to all cosmic-reconstructed muons in this sample and computed alignment quantities from segments within these tracks.

To quantify the alignment of one ring relative to its neighbor, segments in the reference ring were linearly extrapolated to the next ring. The difference in  $r\phi$  position between the extrapolated reference and the observed segment is defined as the  $r\phi$  residual. Peaks in the residuals distribution are fitted with restricted Gaussians, much like the tracker-to-ring procedure. The fact that the segment extrapolation ignores magnetic fields is compensated for by performing peak-fits independently for positively and negatively charged muons and averaging the results. (Positive and negative muons are approximately identified by the sign of the  $q \times p_z$  estimate.) This procedure also relies sensitively on the  $\phi_y$  alignment of chambers, which is derived from about  $3 \text{ pb}^{-1}$  of collisions TrackerMuons (see Jim’s talk at the Oct. 8 Muon Alignment meeting<sup>2</sup>). The resulting residuals biases in bins of  $\phi$  are fitted to Eqn. 1 before and after the tracker-to-ring alignment.

## 4.3 Cross-check results

Beam-halo residuals are presented in  $r\phi$  residual versus  $\phi$  plots for all relevant pairs of rings. Figure 14 shows extrapolations from ME3/1 to ME4/1, Figs. 15 and 16 show ME2/1 to ME3/1 and ME2/2 to 3/2 respectively, which are not expected to have large misalignments even before the tracker-to-muon correction (since they are mounted on the same physical disk). Figures 17–19 present extrapolations from ME2 to ME1/1, 1/2, and 1/3, respectively, where the magnetic field is strongest. Note that beam-halo distributions are not  $\phi$ -symmetric, and that large magnetic fields require larger (and less accurate) cancellation. The vertical scale is wider for Figs. 17–19.

Figure 14 is the most dramatic, showing that even tracker-tracks propagated to the outermost muon station of CMS yield alignment corrections accurate to a few hundred microns, when observed with a completely independent method. Comparisons closer to the tracker are in less perfect agreement, but this is the region where the beam-halo method is inaccurate due to larger magnetic field corrections and lower statistics. The tracker-to-muon alignment, however, must be more accurate closer to the tracker, because incorrectly-propagated tracks can only worsen with distance of propagation.

The fit-values of the curve after alignment is presented in Table 2.

## 5 Stability of internal chamber alignment

In this last section, we revisit the internal chamber alignment in light of the new ring positions and what we learned from the collisions muons that produced it. The internal ring alignment

---

<sup>2</sup><http://indico.cern.ch/conferenceDisplay.py?confId=109787>

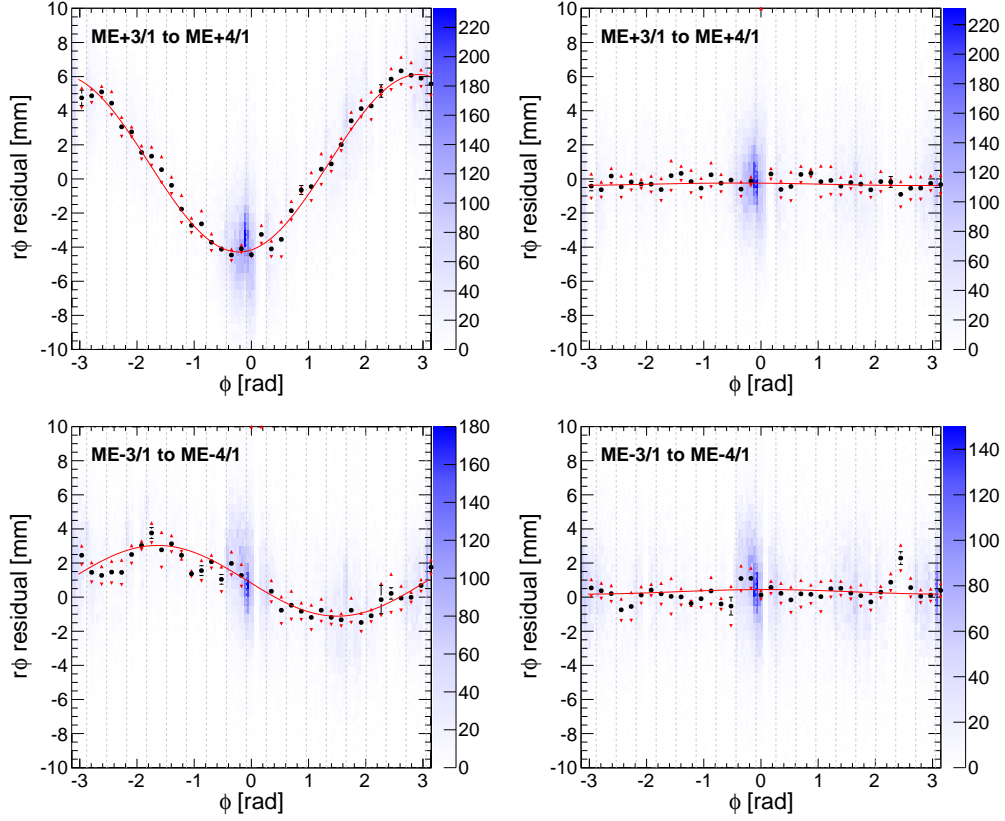


Figure 14: Consistency of beam-halo segments linearly extrapolated from ME3/1 to ME4/1 with segments in ME4/1, before (left) and after (right) the independent tracker-to-muon ring alignment. Red triangles are separate peak fits of positive  $q \times p_z$  muons (upward-pointing triangles) and negative  $q \times p_z$  muons (downward-pointing triangles), and black circles are the averages.

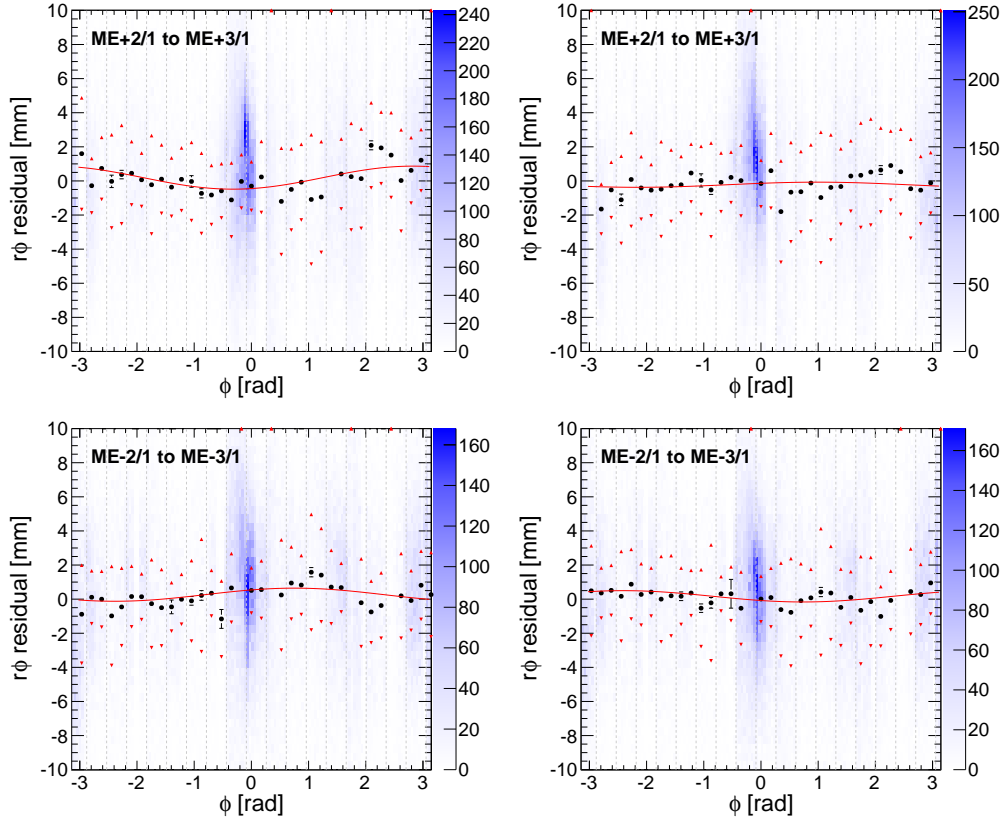


Figure 15: Consistency of beam-halo segments linearly extrapolated from ME2/1 to ME3/1 with segments in ME3/1, before (left) and after (right) the independent tracker-to-muon ring alignment. (See Fig. 14 for additional explanation.) Large corrections were not expected (or observed) before alignment, as the ME2 and ME3 stations are connected to the same physical disk.

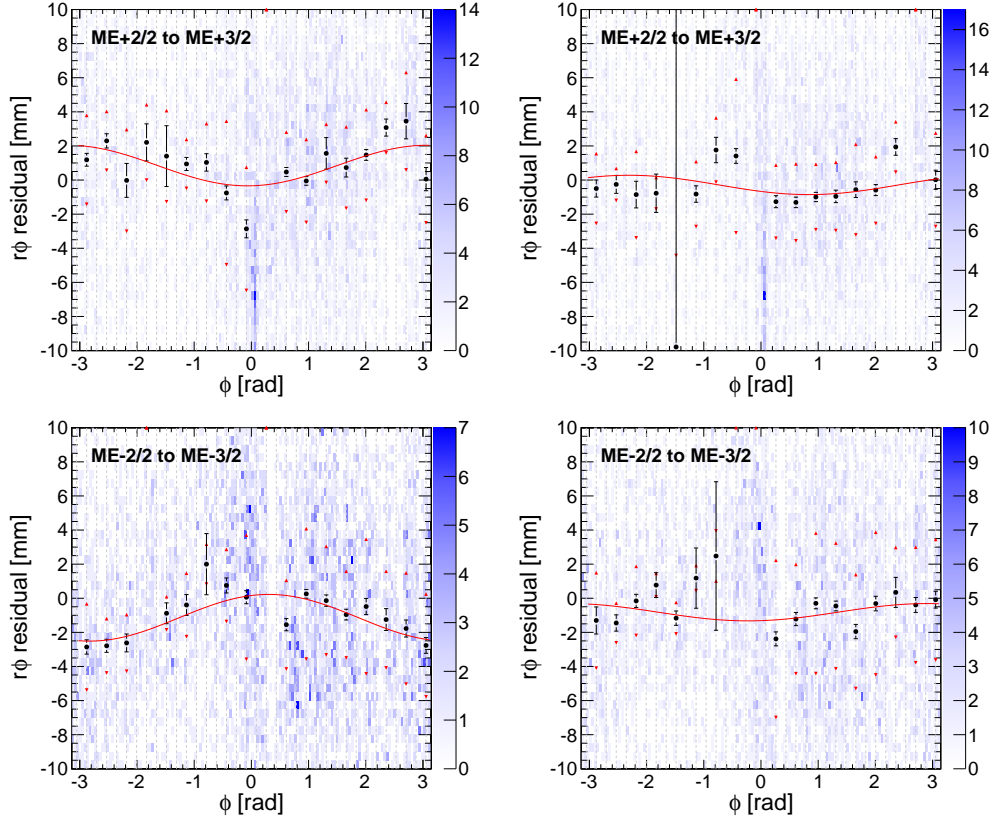


Figure 16: Consistency of beam-halo segments linearly extrapolated from ME2/2 to ME3/2 with segments in ME3/2, before (left) and after (right) the independent tracker-to-muon ring alignment. (See Fig. 14 for additional explanation.) Large corrections were not expected (or observed) before alignment, as the ME2 and ME3 stations are connected to the same physical disk. (Outer rings like ME2/2 and ME3/3 have poor beam-halo statistics.)

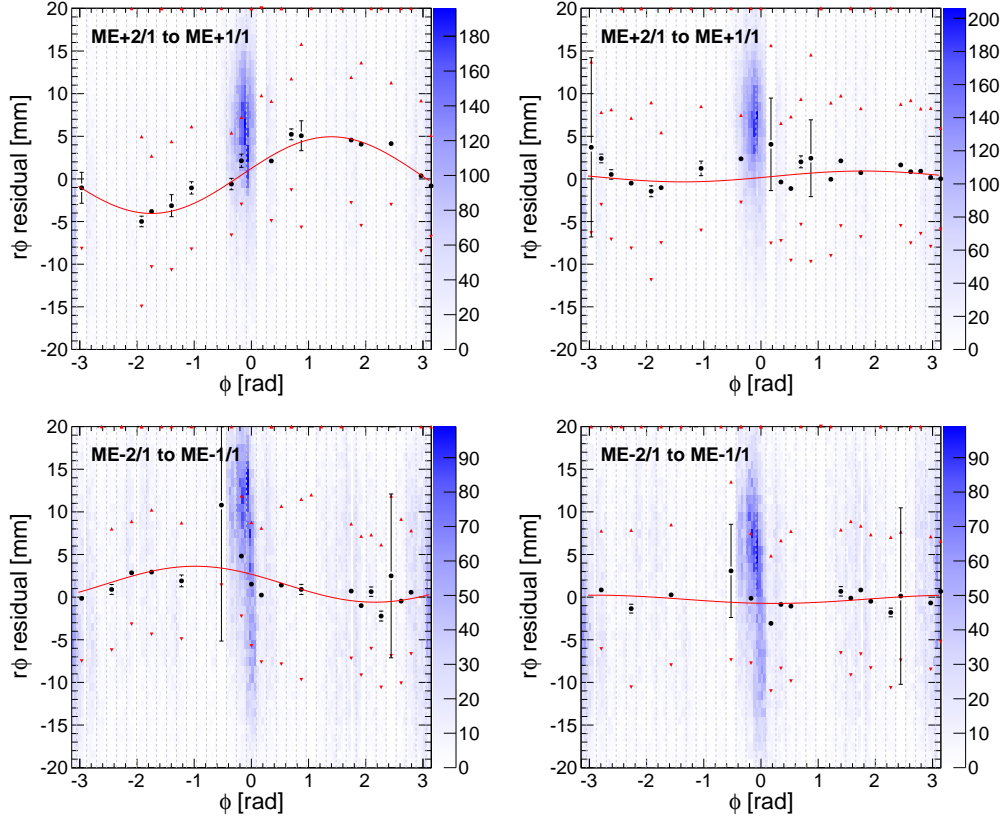


Figure 17: Consistency of beam-halo segments linearly extrapolated from ME2/1 to ME1/1 with segments in ME1/1, before (left) and after (right) the independent tracker-to-muon ring alignment. (See Fig. 14 for additional explanation.) Differences between muons and antimuons (red triangles) are large because the radial magnetic field was not taken into account when propagating segments between stations.

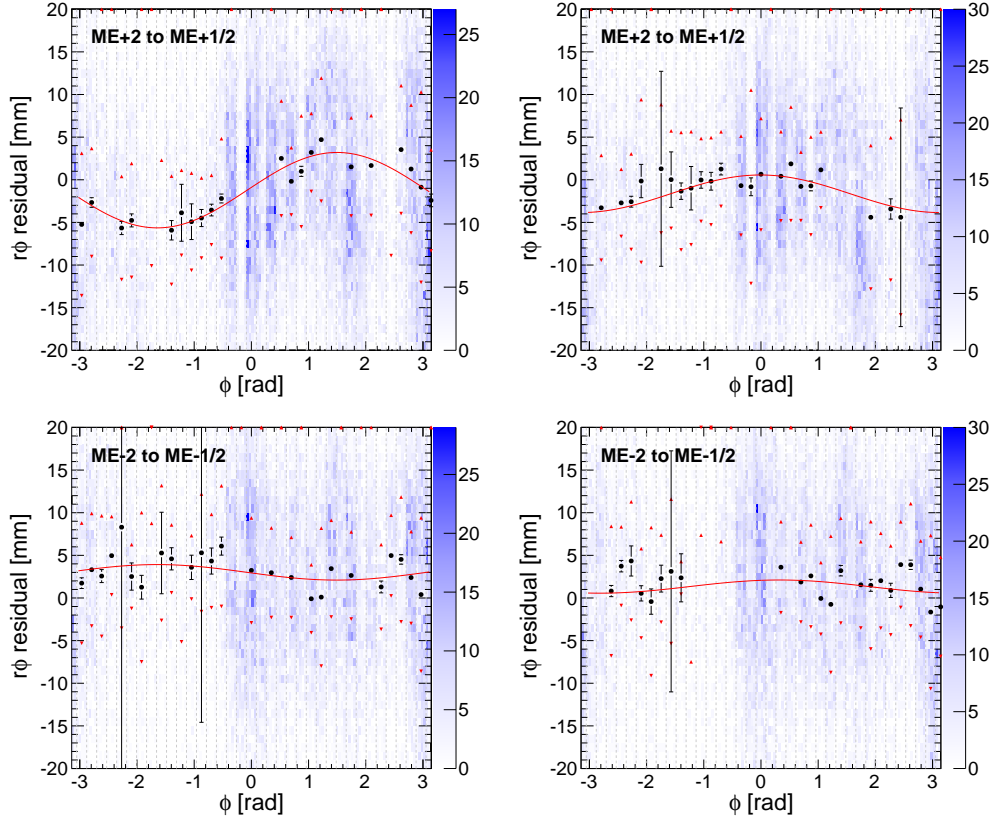


Figure 18: Consistency of beam-halo segments linearly extrapolated from ME2 to ME1/2 with segments in ME1/2, before (left) and after (right) the independent tracker-to-muon ring alignment. (See Fig. 14 for additional explanation.) Differences between muons and antimuons (red triangles) are large because the radial magnetic field was not taken into account when propagating segments between stations. (ME1/2 has poor beam-halo statistics.)

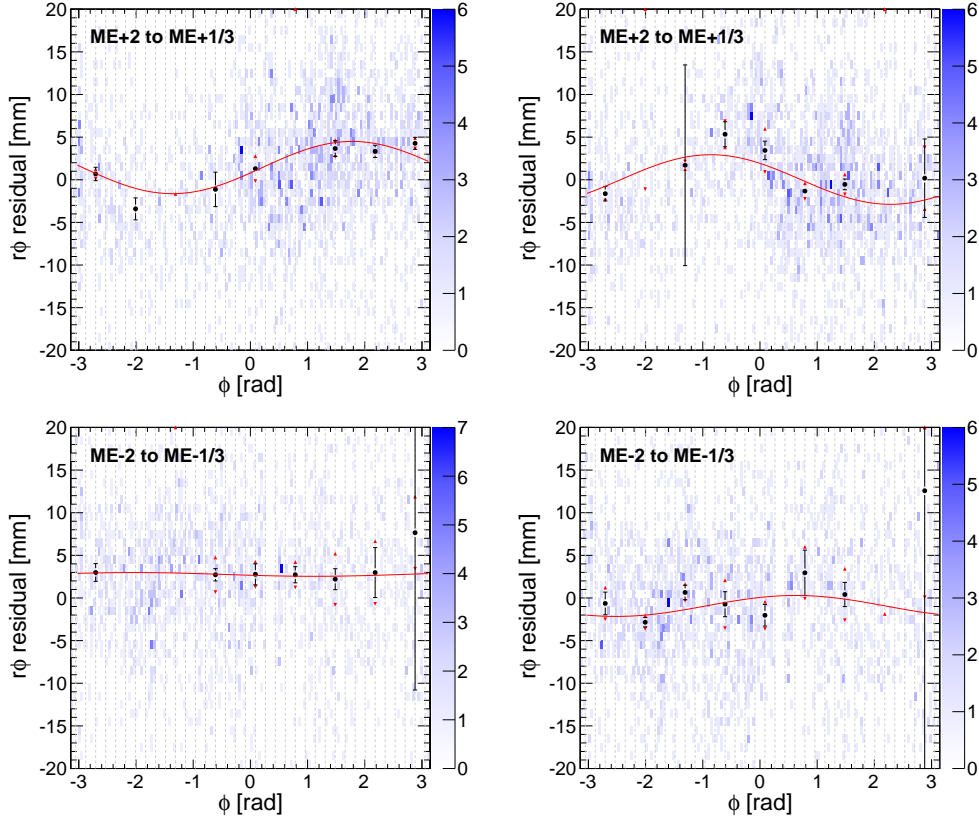


Figure 19: Consistency of beam-halo segments linearly extrapolated from ME2/2 to ME1/3 with segments in ME1/3, before (left) and after (right) the independent tracker-to-muon ring alignment. (See Fig. 14 for additional explanation.) Differences between muons and antimuons (red triangles) are large because the radial magnetic field was not taken into account when propagating segments between stations. (ME1/3 has poor beam-halo statistics.)



Table 2: Fit results with statistical uncertainties for Figs. 14–19, demonstrating the level of agreement between the tracker-to-ring method (Table 1) and the ring-to-ring method.

	$\delta_x$ (mm)	$\delta_y$ (mm)	$\delta_{\phi_z}$ (mrad)	
ME+3/1 $\rightarrow$ ME+4/1	$-0.029 \pm 0.029$	$+0.066 \pm 0.023$	$-0.140 \pm 0.008$	Fig. 14
ME+2/2 $\rightarrow$ ME+3/2	$-0.420 \pm 0.176$	$-0.380 \pm 0.166$	$-0.060 \pm 0.027$	Fig. 16
ME+2/1 $\rightarrow$ ME+3/1	$+0.126 \pm 0.036$	$+0.083 \pm 0.027$	$-0.104 \pm 0.010$	Fig. 15
ME+2/2 $\rightarrow$ ME+1/3	$-2.204 \pm 0.659$	$+1.898 \pm 0.579$	$+0.005 \pm 0.073$	Fig. 19
ME+2 $\rightarrow$ ME+1/2	$-0.012 \pm 0.176$	$+2.203 \pm 0.153$	$-0.511 \pm 0.039$	Fig. 18
ME+2/1 $\rightarrow$ ME+1/1	$+0.621 \pm 0.152$	$-0.129 \pm 0.117$	$+0.153 \pm 0.051$	Fig. 17
ME-2/1 $\rightarrow$ ME-1/1	$-0.116 \pm 0.137$	$-0.469 \pm 0.100$	$-0.133 \pm 0.044$	Fig. 17
ME-2 $\rightarrow$ ME-1/2	$+0.244 \pm 0.214$	$+0.733 \pm 0.135$	$+0.413 \pm 0.048$	Fig. 18
ME-2/2 $\rightarrow$ ME-1/3	$+0.716 \pm 0.710$	$+0.998 \pm 0.740$	$-0.150 \pm 0.090$	Fig. 19
ME-2/1 $\rightarrow$ ME-3/1	$-0.222 \pm 0.038$	$-0.246 \pm 0.026$	$+0.0786 \pm 0.010$	Fig. 15
ME-2/2 $\rightarrow$ ME-3/2	$+0.114 \pm 0.171$	$-0.495 \pm 0.193$	$-0.172 \pm 0.026$	Fig. 16
ME-3/1 $\rightarrow$ ME-4/1	$+0.008 \pm 0.028$	$+0.133 \pm 0.021$	$+0.142 \pm 0.008$	Fig. 14

procedure using beam-halo overlaps is described in detail in the Oct. 29 HyperNews paper.

The first question we should ask is whether the two alignments can truly be factorized: if we re-align the internal geometry starting from the new ring positions, do we obtain the same relative positions? This can be quantified by comparing the chamber positions after the tracker-to-ring alignment but before re-aligning the chambers with beam-halo overlaps. These differences are histogrammed in Fig. 20. Only in ME $\pm$ 1/2 are the differences non-negligible (RMS of 0.8 mm), and these are the only two rings that have antipodal photogrammetry constraints. (The only other ring with more than one photogrammetry constraint is ME+2/2, but these are only 4 chambers apart.) This is relevant because the photogrammetry applies  $r\phi$  position constraints relative to a ring center that is not equal to the ring center derived from the tracker-to-ring alignment. The photogrammetry coordinate frame is allowed to float, but in only one dimension,  $\phi$ , though the ring origin was moved in two dimensions,  $x$  and  $y$ . Thus, the photogrammetry’s coordinate system can pull chambers in the ring if it applies two or more constraints with a significant distance between them. This effect can be seen clearly by plotting these same chamber corrections as a function of chamber number ( $\phi$ ) in Fig. 21: the largest deviation occurs at the constraints with all other chambers interpolating in between.

To avoid this, we can simply apply no more than one photogrammetry constraint per ring. This has the advantage that the photogrammetry effectively becomes a simple two-chamber constraint, since it specifies the locations of neighboring chambers  $A$  and  $B$  relative to an origin  $\mathcal{O}$  which is allowed to float: the only forced condition is for  $A - B$  to have a given value. It has the disadvantage that the network of alignables becomes an unclosed loop: uncertainties grow with distance from the constraint. Figure 22 shows what happens

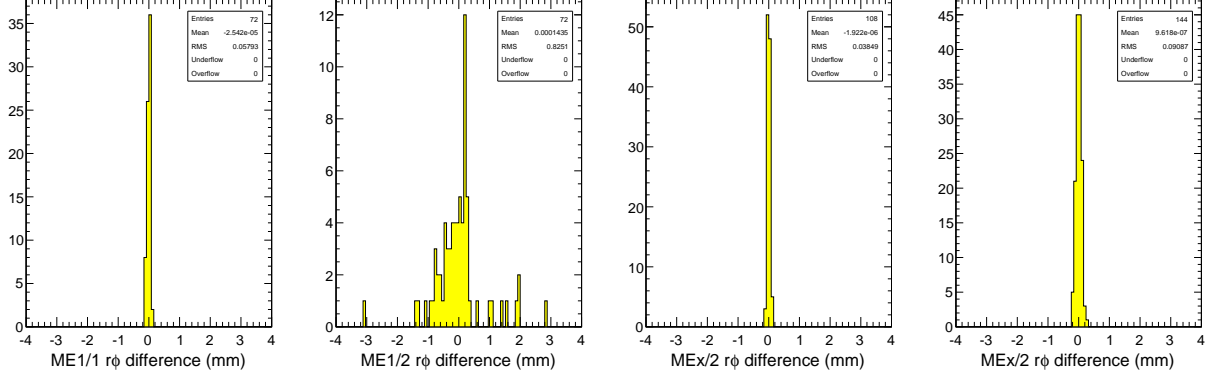


Figure 20: Differences in chamber  $r\phi$  positions before and after re-alignment with the new ring positions. Only ME $\pm$ 1/2 are significantly affected, and these two rings are the only ones with antipodal photogrammetry constraints.

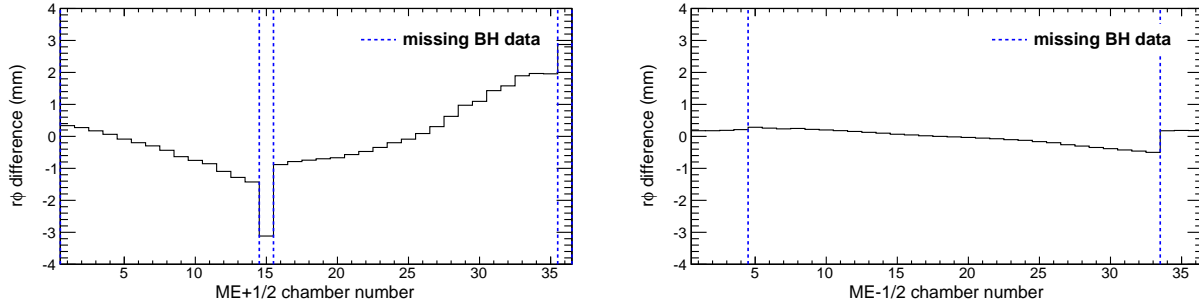


Figure 21: Differences in ME $\pm$ 1/2  $r\phi$  chamber positions (Fig. 20) in greater detail, showing the locations of the missing beam-halo data/photogrammetry constraints. The disks are being distorted by the photogrammetry's coordinate system (a ring position that is different from what was determined by the tracker-to-ring alignment).

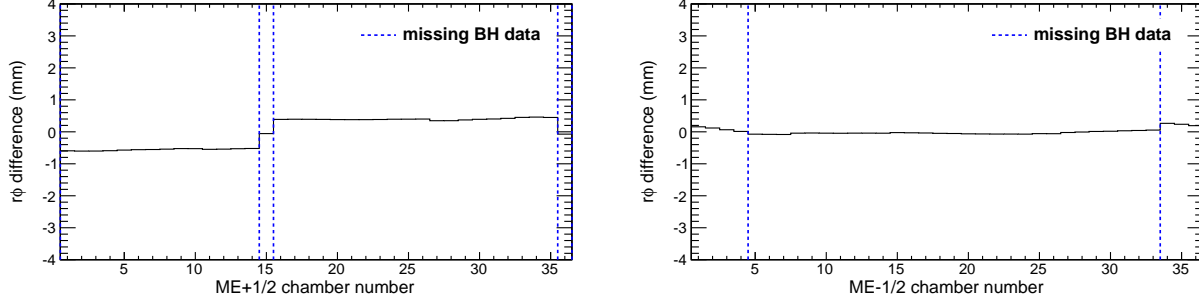


Figure 22: Differences in ME $\pm$ 1/2  $r\phi$  chamber positions with only one photogrammetry constraint per ring: compare to Fig. 21. A constraint was applied in ME+1/2 chambers 14–16 and ME–1/2 chambers 33–34.

to ME $\pm$ 1/2 when only one of the two photogrammetry constraints is required: chambers connected purely by beam-halo measurements are shifted as coherent groups. By applying this looser photogrammetry constraint, the internal ring alignments can be made independent of changes in the overall ring position.

During the tracker-to-ring procedure, large internal misalignments were observed in ME1/1, which was not unexpected, since ME1/1 rings are missing beam-halo data at several points without photogrammetry to fill the gaps. To use this information in a way that minimally depends on tracker-to-muon propagations, one can align the chambers bordering the missing beam-halo data by hand from the collisions data and feed these into the beam-halo overlaps alignment as new constraints. Figure 23 shows the ME1/1 residuals distribution as seen by collisions muons with green boxes highlighting the 12 chambers aligned by hand. Figures 24 and 25 show the effect that these new constraints have on the beam-halo alignment of ME1/1.

In summary, we have made two minor modifications to the beam-halo overlaps alignment procedure, inspired by the collisions residuals:

- now only one group of nearby chambers per ring is constrained by photogrammetry, to avoid imposing the photogrammetry’s coordinate frame on the ring geometry;
- now the ME1/1 beam-halo fit is constrained at six points with measurements derived from collisions residuals.

A list of constrained chambers is given in Table 3. This is the internal ring geometry we propose for sign-off.

## 6 Conclusions: recommended endcap constants

In summary, we have aligned the CSC rings relative to the tracker, independently confirmed their positions using beam-halo muons that cross multiple stations, and have updated the internal alignment of rings in light of observations from the collisions residuals. The updated internal ring alignment is final, to be submitted for approval. The alignment of the rings will need to be repeated using the latest tracker description and cross-alignment, but using exactly the methods described in Sec. 2.

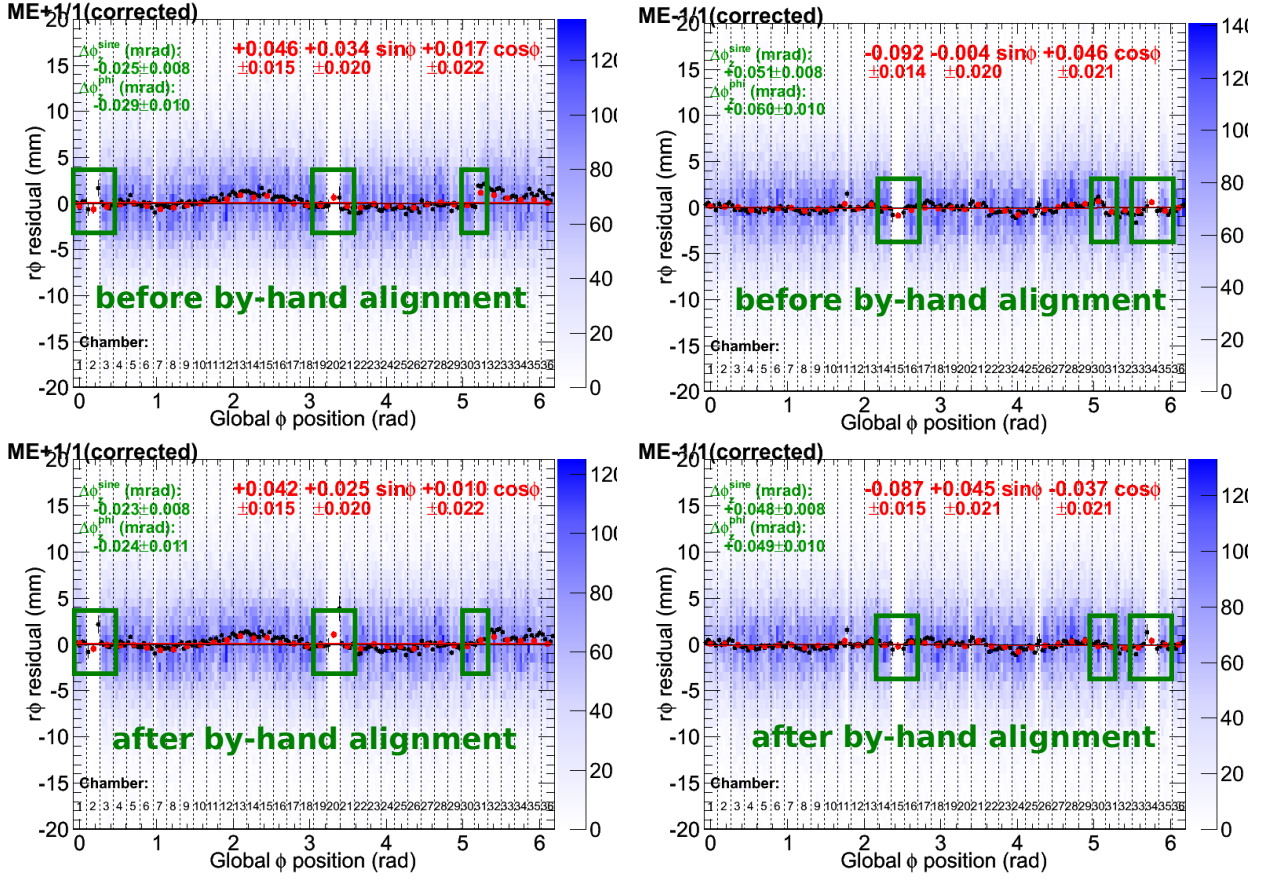


Figure 23: Alignment of 12 chambers by hand using the collisions data. The purpose of this is to provide constraints at key points for the beam-halo overlaps alignment.

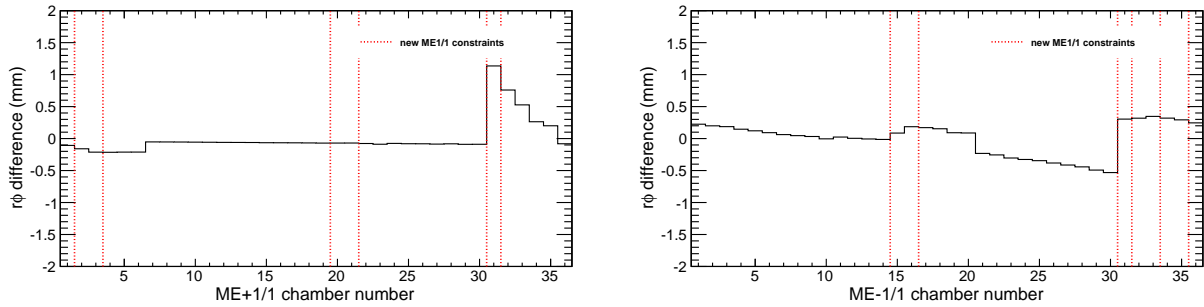


Figure 24: Changes in the beam-halo overlaps alignment caused by the 12 new constraints in ME1/1 ( $r\phi$ ). Since these points had previously been unconstrained by any data, these changes are likely an improvement.

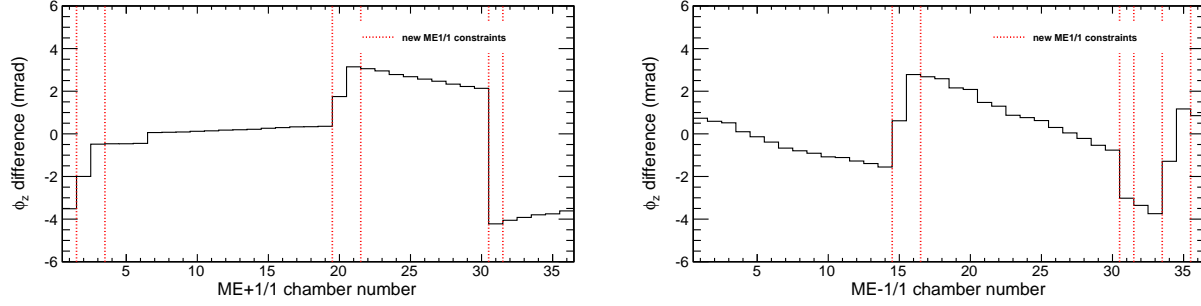


Figure 25: Changes in the beam-halo overlaps alignment caused by the 12 new constraints in ME1/1 ( $\phi_z$ ). Since these points had previously been unconstrained by any data, these changes are likely an improvement.

Table 3: Photogrammetry and collisions data used to constrain final beam-halo overlaps alignment. Only one point in each ring is constrained by photogrammetry, and constraints from collisions data are expressed in the tracker's coordinate system.

Photogrammetry	ME+4/1/14 and ME+4/1/15
constraints	ME+3/2/18 and ME+3/2/19
	ME+2/2/19 and ME+2/2/20
	ME+2/1/01 and ME+2/1/02
	ME+1/2/14, ME+1/2/15, and ME+1/2/16
	ME-1/2/33 and ME-1/2/34
	ME-2/1/06 and ME-2/1/07
	ME-2/2/02, ME-2/2/03, and ME-2/2/04
Constraints from	ME+1/1/01 and ME+1/1/03
TrackerMuon residuals	ME+1/1/19 and ME+1/1/21
	ME+1/1/30 and ME+1/1/31
	ME-1/1/14 and ME-1/1/16
	ME-1/1/33 and ME-1/1/35
	ME-1/1/30 and ME-1/1/31

## 6.1 Provenance of set of constants

The internally aligned CSC geometry can be found here:

`/afs/cern.ch/user/p/pivarski/public/NOV05_PG-HW-phiy-BHPGholes-rings2-BHPGholes2.db`

The following procedures have been applied to this set of constants, in the following order:

1. Photogrammetry: local  $x, y, z, \phi_x, \phi_z$ ;
2. SLM lines for disk displacement and bending due to magnetic field: local  $z, \phi_x$  (replacing PG);
3. “Missing angle measurement” from collisions relative to the tracker: local  $\phi_y$  (see Jim’s talk at the Oct. 8 Muon Alignment meeting<sup>3</sup>);
4. Beam-halo alignment of chambers relative to rings, with PG constraining only the gaps in the beam-halo data (no PG constraint in ME1/1):  $r\phi$  and  $\phi_z$  (replacing PG), see the Oct. 29 HyperNews paper;
5. Ring alignment using collisions: global  $x, y, \phi_z$  of rings, keeping internal chamber structure intact (Sec. 2 of this note);
6. Beam-halo re-alignment of chambers relative to rings, with only one PG constraint per ring and with ME1/1 constraints derived from collisions (Sec. 5 of this note).

## 6.2 Well-defined methods to repeat with the latest tracker and cross-alignments

Now that these procedures have been defined, they must be repeated with the new tracker alignment and tracker/muon system cross-alignment. The following will be performed with the latest tracker description (calibration and alignment) and cross-alignment results (GlobalAlignmentRcd):

1. Re-run the tracker-to-ring alignment exactly as it was done here, updating global ring parameters only.
2. Verify that the updates are smaller than 1 mm, 1 mrad or are consistent with a global translation/rotation.
3. Submit the resulting geometry for approval before Nov. 12, but likely much sooner.
4. When approved, upload it to the database and notify the Muon POG for testing.

---

<sup>3</sup><http://indico.cern.ch/conferenceDisplay.py?confId=109787>